The Astrophysical Journal, 701:32–41, 2009 August 10 doi:10.1088/0004-637X/701/1/32

GALAXY CLUSTERS DISCOVERED WITH A SUNYAEV–ZEL'DOVICH EFFECT SURVEY

Z. Staniszewski[1,2], P. A. R. Ade[3], K. A. Aird[4], B. A. Benson[5], L. E. Bleem[6,7], J. E. Carlstrom[6,7,8,9], C. L. Chang[6,9], H.-M. Cho[5], T. M. Crawford[6,8], A. T. Crites[6,8], T. de Haan[10], M. A. Dobbs[10], N. W. Halverson[11], G. P. Holder[10], W. L. Holzapfel[5], J. D. Hrubes[4], M. Joy[12], R. Keisler[6,7], T. M. Lanting[10], A. T. Lee[5,13], E. M. Leitch[6,8], A. Loehr[14], M. Lueker[5], J. J. McMahon[6,9], J. Mehl[5], S. S. Meyer[6,7,8,9], J. J. Mohr[15], T. E. Montroy[1,2], C.-C. Ngeow[15], S. Padin[6,8], T. Plagge[5], C. Pryke[6,8,9], C. L. Reichardt[5], J. E. Ruhl[1,2], K. K. Schaffer[6,9], L. Shaw[10], E. Shirokoff[5], H. G. Spieler[13], B. Stalder[14], A. A. Stark[14], K. Vanderlinde[6,8,9], J. D. Vieira[6,7], O. Zahn[16], and A. Zenteno[15]
[1] Physics Department, Case Western Reserve University, Cleveland, OH 44106, USA
[2] Center for Education and Research in Cosmology and Astrophysics, Case Western Reserve University, Cleveland, OH 44106, USA
[3] Department of Physics and Astronomy, Cardiff University, CF24 3YB, UK
[4] University of Chicago, 5640 South Ellis Avenue, Chicago, IL 60637, USA
[5] Department of Physics, University of California, Berkeley, CA 94720, USA
[6] Kavli Institute for Cosmological Physics, University of Chicago, 5640 South Ellis Avenue, Chicago, IL 60637, USA; tcrawfor@kicp.uchicago.edu
[7] Department of Physics, University of Chicago, 5640 South Ellis Avenue, Chicago, IL 60637, USA
[8] Department of Astronomy and Astrophysics, University of Chicago, 5640 South Ellis Avenue, Chicago, IL 60637, USA
[9] Enrico Fermi Institute, University of Chicago, 5640 South Ellis Avenue, Chicago, IL 60637, USA
[10] Department of Physics, McGill University, 3600 Rue University, Montreal, Quebec H3A 2T8, Canada
[11] Department of Astrophysical and Planetary Sciences and Department of Physics, University of Colorado, Boulder, CO 80309, USA
[12] Department of Space Science, VP62, NASA Marshall Space Flight Center, Huntsville, AL 35812, USA
[13] Physics Division, Lawrence Berkeley National Laboratory, Berkeley, CA 94720, USA
[14] Harvard-Smithsonian Center for Astrophysics, 60 Garden Street, Cambridge, MA 02138, USA
[15] Department of Astronomy and Department of Physics, University of Illinois, 1002 West Green Street, Urbana, IL 61801, USA
[16] Berkeley Center for Cosmological Physics, Department of Physics, University of California, and Lawrence Berkeley National Labs, Berkeley, CA 94720, USA
Received 2008 October 10; accepted 2009 June 8; published 2009 July 20

ABSTRACT

The South Pole Telescope (SPT) is conducting a Sunyaev–Zel'dovich (SZ) effect survey over large areas of the southern sky, searching for massive galaxy clusters to high redshift. In this preliminary study, we focus on a 40 deg^2 area targeted by the Blanco Cosmology Survey (BCS), which is centered roughly at right ascension 5^h30^m, declination -53° (J2000). Over two seasons of observations, this entire region has been mapped by the SPT at 95 GHz, 150 GHz, and 225 GHz. We report the four most significant SPT detections of SZ clusters in this field, three of which were previously unknown and, therefore, represent the first galaxy clusters discovered with an SZ survey. The SZ clusters are detected as decrements with greater than 5σ significance in the high-sensitivity 150 GHz SPT map. The SZ spectrum of these sources is confirmed by detections of decrements at the corresponding locations in the 95 GHz SPT map and nondetections at those locations in the 225 GHz SPT map. Multiband optical images from the BCS survey demonstrate significant concentrations of similarly colored galaxies at the positions of the SZ detections. Photometric redshift estimates from the BCS data indicate that two of the clusters lie at moderate redshift ($z \sim 0.4$) and two at high redshift ($z \gtrsim 0.8$). One of the SZ detections was previously identified as a galaxy cluster in the optical as part of the Abell supplementary southern cluster catalog and in the X-ray using data from the *ROSAT* All-Sky Survey (RASS). Potential RASS counterparts (not previously identified as clusters) are also found for two of the new discoveries. These first four galaxy clusters are the most significant SZ detections from a subset of the ongoing SPT survey. As such, they serve as a demonstration that SZ surveys, and the SPT in particular, can be an effective means for finding galaxy clusters.

Key words: cosmic microwave background – cosmology: observations – galaxies: clusters: general

1. INTRODUCTION

Galaxy clusters are the most massive collapsed objects in the universe, and measurements of their abundance and evolution can be used to place constraints on cosmological models. In particular, the abundance of clusters as a function of redshift depends on both the growth of structure and the volume of space. A catalog of clusters with masses and redshifts can be used to constrain the matter density, the density fluctuation amplitude, and the dark energy equation of state (Wang & Steinhardt 1998; Haiman et al. 2001; Holder et al. 2001; Molnar et al. 2004; Wang et al. 2004; Lima & Hu 2007).

For a galaxy cluster catalog to be useful for constraining cosmological models, the sample of clusters must be selected in a uniform and well-understood manner (Melin et al. 2005). In addition, cluster parameters—mass, in particular—must be estimable from the observed quantities. Galaxy cluster catalogs selected via the Sunyaev–Zel'dovich effect are promising in both respects (Carlstrom et al. 2002; Majumdar & Mohr 2004; Melin et al. 2005).

The Sunyaev–Zel'dovich (SZ) effect is the inverse-Compton scattering of cosmic microwave background (CMB) photons by hot plasma bound to clusters of galaxies, which results in a distortion of the CMB blackbody spectrum (Sunyaev & Zeldovich 1970, 1972). The spectrum of the SZ effect has a null at ~217 GHz, where there is no net distortion and the intensity remains unchanged. At frequencies below ~217 GHz, the spectral distortion results in a decrement in the CMB intensity in the direction of the galaxy cluster.

As it is a distortion of the CMB spectrum, the surface brightness of the SZ effect does not depend on cluster distance. Observations of the SZ effect, therefore, permit the detection

of clusters with a selection function that is nearly redshift-independent (Birkinshaw 1999; Carlstrom et al. 2002). The amplitude of the SZ spectral distortion is proportional to the integrated pressure along the line of sight through the cluster, and the relationship between integrated SZ flux and cluster mass is expected to have relatively low scatter (Motl et al. 2005; Nagai 2006; Shaw et al. 2008). Therefore, an SZ-flux-limited survey, combined with redshifts from optical observations, has the potential to be a nearly ideal data set for producing cosmological constraints.

Significant SZ detections of previously known clusters have been reported in many tens of X-ray and optically selected galaxy clusters with observations spanning from radio to submillimeter wavelengths (e.g., Jones et al. 2005; Bonamente et al. 2006; Benson et al. 2004; Halverson et al. 2009). However, despite the promise of SZ surveys for cosmology, there has been only one reported detection of the SZ effect in a field not already suspected to harbor a cluster. A deep survey of a relatively small field with the VLA at 8.4 GHz produced what appeared to be a significant flux decrement (Richards et al. 1997). However, subsequent BIMA observations at 30 GHz were found to be inconsistent with the interpretation of the VLA decrement as being due to the SZ effect (Holzapfel et al. 2000).

The South Pole Telescope (SPT) is the first instrument to demonstrate the requisite combination of resolution, mapping speed, and observing time to carry out a successful search for distant galaxy clusters through the SZ effect. This paper presents the four most significant detections of SZ clusters in a preliminary analysis of a $\sim$40 deg^2 subset of the SPT survey area.

A brief description of the telescope and receiver and descriptions of the SPT observations, data reduction, and cluster-searching algorithms are found in Section 2. The cluster candidates are presented in Section 3, including a discussion of possible X-ray counterparts in Section 3.1 and optical follow-up observations in Section 3.2. Finally, we summarize the main results of this work in Section 4.

2. INSTRUMENT, OBSERVATIONS, AND DATA REDUCTION

2.1. Instrument

The SPT is a 10 m diameter off-axis telescope optimized for observations of fine angular scale CMB anisotropy (Ruhl et al. 2004; Padin et al. 2008; Carlstrom et al. 2009). The SPT receiver is equipped with a 960-element array of superconducting transition edge sensor (TES) bolometers, read out by a frequency-domain-multiplexed system using superconducting quantum interference device (SQUID) amplifiers. This array is made up of six subarrays, each of which can be configured to observe in one of the 95, 150, or 225 GHz atmospheric windows. For the observations used in this paper, the fractional bandwidths in the three observing bands were $\sim$30% at 95 GHz, $\sim$25% at 150 GHz, and $\sim$22% at 225 GHz.

The main lobes of the beams in the final maps used in this paper are reasonably approximated by two-dimensional elliptical Gaussians with average full widths at half-maximum (FWHM) of 1.5, 1.2, and 1.1 arcmin for 95, 150, and 225 GHz. These are larger than would be naively calculated from the aperture diameter and observing wavelength due to the combination of an underilluminated primary (to reduce spillover) and telescope pointing uncertainty. (See Section 2.3.4 and Padin et al. (2008) for details.) There is evidence in observations of very bright sources for a large ($\sim$20′ radius), low-amplitude (~ -35 dB) sidelobe, accounting for up to 20% of the degree-scale beam response, but this sidelobe should have no impact on the arcminute scales important for the cluster detections presented here (and indeed, including it in the analysis in this work results in percent-level changes in the results).

In a typical observation used in this paper, the instantaneous per-detector sensitivity in the three bands was $\sim$500 $\mu K_{\rm CMB}\sqrt{\rm s}$ at 150 GHz and $\sim$1000–1500 $\mu K_{\rm CMB}\sqrt{\rm s}$ at 95 and 225 GHz.[17]

2.2. Observations

The SPT has begun an extensive survey of the high-galactic-latitude sky visible from the South Pole. The results presented in this work are based on observations of a single field, using data collected over two seasons. In the combined data set, the field is fully covered in our three frequency bands. For each of the few hundred individual observations,[18] initial data cuts are performed, various timestream processing steps are applied, and a single map is made using the data from all selected detectors in a given observing band. The maps from each individual observation are combined to produce a single map of the observed region in each band. Details of the data reduction up to the final maps are given in Section 2.3. Finally, the most sensitive single-frequency map is searched for SZ cluster candidates using a matched-filter technique, the details of which are given in Sections 2.4 and 2.5.

The observations included in this analysis were performed during the 2007 and 2008 SPT observing seasons, using a different focal plane configuration each season. Both the 2007 and 2008 focal planes included detectors sensitive to radiation within bands centered at approximately 95 GHz, 150 GHz, and 225 GHz. Details of the telescope design and performance, focal-plane configuration, and observing strategy for these two seasons are described in Carlstrom et al. (2009). During the 2007 Austral Winter, the SPT began a survey of a $\sim$40 deg^2 field that was also targeted by the Blanco Cosmology Survey[19] (BCS) project. This field is centered roughly at right ascension (R.A.) $5^{\rm h}30^{\rm m}$, declination (decl.) -53° (J2000) and is hereafter referred to as the BCS5h30 field. The observations of the BCS5h30 field with the 2007 SPT focal plane that are included in this paper took place between 2007 July 27 and September 19, for a total of 280 hr of observing time. From this period, we use only the 95 GHz data taken with detectors that passed a set of performance cuts, yielding a median of 129 well-performing detectors per observation.

Between 2008 February 29 and June 5, a $\sim$90 deg^2 field including the BCS5h30 field was observed with the 2008 SPT focal plane. For this paper, we include 607 hr of observing time on the $\sim$90 deg^2 field with a median of 322 good 150 GHz detectors and 170 good 225 GHz detectors. We report results only for the subset of this larger field that overlaps the BCS5h30 field.

The observations reported here were performed using constant-elevation scans across the field. In this scan strategy, the entire telescope is swept at constant angular velocity in azimuth from one edge of the field to the other, and then back.

[17] Throughout this work, $K_{\rm CMB}$ refers to equivalent CMB fluctuation temperature, i.e., the fluctuation on top of a 2.73 K blackbody in the sky that would produce the equivalent signal at the detector.

[18] In this work, we refer to an observation as a single-pass map of the entire field.

[19] http://cosmology.uiuc.edu/BCS/

After each such pair of scans across the field, the telescope executes a step in elevation before performing the next pair. A scanning speed of 0.84 deg of azimuth per second and a scan throw of 13.5 deg of azimuth were chosen for the 2007 observations presented here, resulting in a total scan length of 38.7 s (including turnarounds). The 2008 observations employed two different scan speeds, 0.44 and 0.48 deg of azimuth per second and a scan length of 17.5 deg in azimuth, resulting in total scan lengths of 75–80 s (including turnarounds). The size of the elevation step between pairs of scans was 0.07 deg for the 2007 observations and 0.125 deg for the 2008 observations. A map of the entire field is made using this strategy, and we refer to such a single-pass map as a single observation. One observation takes up to 2 hr. The short time period for a single observation allows for a conservative schedule of interleaved calibrations and facilitates data selection and reduction. Each individual observation produces a fully sampled map of the field, but not fully sampled by each individual detector. A series of different starting elevations are used for successive observations to provide even, fully sampled, coverage of the field over several days.

Between individual observations of the field, we perform a series of short calibration measurements described in more detail in Carlstrom et al. (2009). These include measurements of a chopped thermal source, ∼2 deg elevation nods, and scans across the galactic H II regions RCW38 and MAT5a. This series of regular calibration measurements allows us to identify detectors with good performance, assess relative detector gains, monitor atmospheric opacity and beam parameters, and constrain pointing variations.

2.3. Data Reduction

For this initial cluster-finding analysis, a preliminary data reduction pipeline was developed that provides maps of the BCS5h30 field that are well understood, but not yet optimized. Details of the data processing as presented below are subject to improvement for future analysis.

2.3.1. Data Selection and Notch Filtering

The first step in the data reduction process is to identify the data that will be included in each single-observation map. For every observation, a set of well-performing detectors is identified, primarily by assessing each detector's response to the chopped thermal source, its response to atmospheric emission during the ∼2 deg elevation nods, and its noise in the frequency band appropriate for cluster signals. Performance is also assessed based on the shape of the individual detector's noise power spectrum. If the power spectrum has too many lines or other deviations from the expected functional form, that detector is omitted from that observation's analysis. The median number of detectors stated in Section 2.2 is obtained after the application of these criteria.

In addition to cutting all data from individual detectors with anomalous noise power spectra, a small amount of bandwidth is cut from all detectors in certain observations. The receiver exhibits sensitivity to the pulse-tube cooler, resulting in occasional lines in the detector noise power spectra at frequencies corresponding to the pulse-tube frequency (approximately 1.6 Hz) and its harmonics. In every observation, all detectors' noise power spectra are combined in quadrature, and a search is performed for features in the resulting spectrum at every harmonic of the pulse-tube frequency. If a high-significance feature is found at any harmonic, a notch filter around that harmonic is applied to every detector's timestream. The width of the notch is determined by the fit, with a maximum of 0.007 Hz full width. The maximum amount of bandwidth that could be cut with this filter is 0.4%, but the actual amount is far smaller.

The data are eventually parsed into individual azimuth scans and are further selected for inclusion in the analysis on a scan-by-scan basis. Only the constant-azimuthal-velocity portion of each scan is eligible for inclusion; data taken while the telescope is accelerating are omitted. Scans during which there were data acquisition problems or large (>20 arcsec) instantaneous pointing errors—roughly 5% of total scans—are flagged for omission. For each detector, data from an individual scan are flagged if the detector or its associated readout channel exhibits high noise, if the demodulated detector output comes close to the limits of the analog-to-digital converter, if the readout SQUID associated with the detector exhibits an anomalously large DC offset, or if the detector demonstrates any cosmic-ray-like events in its time-ordered data. Typically about 5% of all otherwise well-performing bolometers are flagged within a given scan for one of these reasons. Data that remain unflagged after all of these cuts have been applied are processed and included in the maps.

Finally, individual observations are assessed for quality before inclusion in the final coadded maps. Observations are excluded if the thermal conditions of the receiver were not sufficiently stable, if the number of well-performing detectors was anomalously low, or if the observation was not fully completed. Individual observation maps are also excluded from the final maps if the rms in the single-observation map exceeds an empirically determined threshold. Of the complete observations of the BCS5h30 field, approximately 77% (270/350) of the 2007 observations and 83% (314/377) of the 2008 observations are included in the final maps.

2.3.2. Relative and Absolute Calibration

The relative gains of the detectors, and their gain variations over time, are estimated using measurements of their response to a chopped thermal source taken before every observation. This relative calibration is used to "flat-field" the array before estimation of any common-mode timestream signal and before mapmaking. For the relative calibration step before mapmaking, we apply corrections to account for variations in illumination of the thermal source across the focal plane. These are measured by calculating the ratio of each detector's response to the thermal source to its response to the galactic H II region RCW38, averaged over many measurements.

We convert the RCW38-corrected relative calibration into an absolute calibration by comparing our measurements of RCW38 with published flux measurements in our observing bands. For 150 and 225 GHz, we compare to the RCW38 flux reported by ACBAR (Runyan et al. 2003), which was recently linked to the WMAP5 calibration at 150 GHz (Reichardt et al. 2009). In order to use the ACBAR calibration, we smooth the SPT map of RCW38 to match the ACBAR resolution. We then compare the flux within the inner 8 arcmin of the SPT map with the ACBAR-determined flux. For the 95 GHz calibration, we use the flux reported by BOOMERANG (Coble et al. 2003). In this case, we smooth the SPT RCW38 map to match the BOOMERANG resolution and then compare the flux within two times the Gaussian width (σ) of the BOOMERANG beam.

This calibration method does not correct for temporal variations in atmospheric opacity between SPT measurements of RCW38. This results in a slightly suboptimal weighting of detectors during mapmaking, but does not bias the absolute calibration. The added absolute calibration uncertainty from

ignoring atmospheric opacity corrections is small relative to our overall calibration uncertainty. For each of our bands over both seasons, the rms variation in the brightness of RCW38 is measured to be <5%, even without correcting for differences in atmospheric opacity or changes in the relative response of the bolometers.

We estimate the calibration uncertainty of the 95, 150, and 225 GHz bands to be 13%, 8%, and 16%, respectively. At these levels of uncertainty, the RCW38-based calibration is consistent with other cross-checks of our calibration, including initial CMB power spectrum estimates and observations of Neptune.

2.3.3. Timestream Processing

In addition to the notch filtering described in Section 2.3.1, the timestream processing of detector data consists of deconvolution of the detector response function, low-pass filtering, and projecting out long-timescale drifts due to atmosphere and readout $1/f$ noise.

Detector-response deconvolution and low-pass filtering are done in a single step. The detector temporal-response functions are measured periodically by sweeping the chop frequency of the thermal calibration source and measuring the amplitude and phase of each detector's response. These temporal-response functions are fit adequately by a single-pole low-pass filter, and the time constants do not vary significantly from observation to observation. Across the focal plane, the time constants ranged from 5 to 10 ms in 2007 and from 10 to 20 ms in 2008. The cutoff for the applied low-pass filter is set at 40 Hz for the 2007 data and 25 Hz for the 2008 data, such that in conjunction with a digital filter already applied by the data acquisition computer, they filter approximately the same spatial scales ($\lesssim 0.5$ arcmin), given the different scan speeds for each season. This combination acts as an anti-aliasing filter for our eventual resampling of the data onto 0.25 arcmin map pixels but does not suppress power on scales of the SPT beams.

For every scan, each detector's timestream is then fit simultaneously to a number of slowly varying template functions, and the best fit to each template is subtracted from that detector's timestream. This time-domain filter reduces the effect of low-frequency noise in the detector timestreams due to readout noise or to atmospheric fluctuations. For this analysis, we use a combination of Legendre polynomials and an array common mode as the templates. The highest order of Legendre polynomial used is 19 for the 2008 data and 11 for the 2007 data, resulting in a characteristic filter scale of roughly one-half degree for both seasons.

The common-mode template is constructed from the mean across all the well-performing detectors in the array at a given observing frequency, using a nominal relative calibration. Removing this common mode should eliminate the majority of the atmospheric fluctuation power in the detector timestreams, because this atmospheric signal is highly correlated between detectors. The common-mode subtraction acts as a spatial high-pass filter with a characteristic scale that roughly corresponds to the 1 deg angular size of the array.

In order to avoid contamination of the best-fit common mode and polynomial by bright point sources, sources were detected in a preliminary set of maps, and the locations of those sources were masked in the common mode and polynomial subtraction algorithm. A total of 92 sources were masked in this analysis, 35 of which lie in the ~40 deg^2 BCS5h30 field. A mask radius of 5 arcmin was used for the five brightest sources (including the three brightest in the BCS5h30 field), and a mask radius of 2 arcmin was used for the rest.

2.3.4. Mapmaking and Pointing Corrections

For every observation, a map is made for each observing frequency using the processed data for all detectors in that band. Pointing information (R.A. and decl.) is calculated for each detector using focal-plane offsets measured in observations of the galactic H II regions, and boresight pointing calculated using data from the telescope pointing readout system, with a set of corrections described below. Pointing coordinates are converted to pixel number using a Sanson–Flamsteed projection (Calabretta & Greisen 2002) with 0.25 arcmin pixels, and all measurements of a given pixel's brightness are averaged using inverse-variance weighting based on the rms of each detector's processed and relative-gain-scaled time-ordered data.

Small corrections must be applied to the pointing information in the timestream to ensure that pointing errors are suitably small compared to the size of the SPT beams. The largest pointing errors of the SPT are attributed to thermal gradients across the telescope support structure. These pointing errors are corrected from 20 arcsec rms to better than 8 arcsec rms by using an offline model which incorporates information from thermal and linear displacement sensors on the telescope structure and observations of H II regions. The astrometry of the pointing model is tied to the PMN and SUMSS catalogs (Wright et al. 1994; Mauch et al. 2003) and is accurate to 10 arcsec in the final maps. The main-lobe beams in the final maps are well approximated by two-dimensional elliptical Gaussians with average FWHM of 1.5, 1.2, and 1.1 arcmin for 95, 150, and 225 GHz. As the beams include the effects of pointing variations and the timestream filtering, they are larger than expected from the diffraction of the central 8 m diameter region of primary mirror illuminated by the SPT-SZ optics (see Padin et al. 2008).

2.4. Identifying Galaxy Cluster Candidates

In this initial analysis, we identify the highest significance cluster candidates using only the 150 GHz map, which has the highest sensitivity. The maps at the other two frequencies are used to provide a cross-check of the cluster detections. The cluster thermal SZ signal should nearly vanish in the 225 GHz map, while the 95 GHz map can be used to confirm the detected clusters. We enhance the signal-to-noise in the SPT maps for sources with morphologies similar to that expected for SZ galaxy clusters through the application of matched spatial filters (Haehnelt & Tegmark 1996; Herranz et al. 2002a, 2002b; Melin et al. 2006). The matched filter, which we apply in the Fourier domain, combines knowledge of the source template with a noise estimate to optimize the signal-to-noise of the source in the filtered map:

$$\psi = \frac{S^T N^{-1}}{\sqrt{S^T N^{-1} S}}, \quad (1)$$

where ψ is the matched filter, N is the noise covariance matrix (including non-SZ astrophysical sources), and S is the assumed source template.

2.4.1. Source Templates

The optimal choice for the source template is unclear for SZ clusters, so we explore three basic profiles, all motivated by some guess at the underlying three-dimensional pressure profile of clusters: a modified version of the Navarro–Frenk–White (NFW; Navarro et al. 1996, 1997) model as suggested in

Nagai et al. (2007), numerically integrated along the line of sight to produce a model for the SZ surface brightness; a Gaussian profile; and a β-model with β between 2/3 and 4/3, which can be analytically integrated to yield the SZ surface brightness. The three models proved almost indistinguishable in terms of detecting the highly significant clusters presented in this work. The results in Section 3 are based on a spherical β-model with $\beta = 1$. The SZ surface brightness profile using a β-model is given by

$$\Delta T_{\rm SZ}(\theta) = \Delta T_0 (1 + \theta^2/\theta_{\rm core}^2)^{(1-3\beta)/2}, \quad (2)$$

where θ is the angular distance from the line of sight through the center of the cluster, $\theta_{\rm core}$ is the (angular) core radius, and ΔT_0 is the peak signal. We choose to fix β and vary $\theta_{\rm core}$, as these two parameters are highly degenerate in the fit, given the current depth and resolution of our observations. The model is truncated at $10 \times \theta_{\rm core}$. We have explored the dependence on the scale size, parameterized as $\theta_{\rm core}$ in the range from 0.′25 to 3.′5 in 0.′25 steps, and generated a matched filter of each case.

The timestream filtering described in Section 2.3.3 affects the expected shape of the cluster signal in our maps. To account for this effect, we convolve the source templates with a spatial filter intended to represent the map-domain version of our timestream filtering before including the source templates in the matched filter for cluster detection. (The source templates are also convolved with the instrument beam). The spatial filter used in this work is simply a high-pass in the R.A. direction, with a cutoff on roughly half-degree scales. Simulations of the timestream filtering have shown this to be an accurate representation of the effect of our timestream polynomial removal. We do not attempt to include the effects of our common-mode subtraction, which predominantly affects modes that will be heavily de-weighted in the matched filter by the inclusion of the primary CMB as a noise term.

2.4.2. Noise and Foreground Estimates

In addition to the SZ signal from massive clusters, SPT maps contain primary CMB, instrument and atmospheric noise, point sources, and an unresolved SZ background. For cluster detection, all of these are noise sources. The covariance matrix used to create the optimal matched filter can be expressed as the sum, $N = N_{\rm CMB} + N_{\rm noise} + N_{\rm PS} + N_{\rm SZ}$, of these components. The point-source covariance only includes the unresolved source background; point sources bright enough to be detected in our maps are treated separately as discussed below.

The signal covariance of the primary CMB and undetected point sources is estimated analytically from the best-fit WMAP5 CMB power spectrum (Nolta et al. 2009) and the Borys et al. (2003) model for dusty point sources. We assume that the contribution of faint radio sources to the background source covariance is negligible. We assume a spectral index of 2.7 to extend the dusty source counts to 150 GHz. The power spectrum of this source count distribution is estimated with the formalism in White & Majumdar (2004). The SZ background covariance is estimated from the simulations described in Shaw et al. (2008).

A different approach is taken for the bright point sources in the map. Any bright sources left in our map will cause ringing in the maps due to the matched filter used, which can give spurious high significance decrements in their vicinity. We take advantage of the fact that these sources show up as bright spots in our maps, while any SZ cluster will be a decrement at 150 GHz. We filter the 150 GHz map using a simple matched filter assuming isotropic noise and no signal filtering, and we flag every positive source above 5σ in the filtered map, totaling 47 sources in the $\sim$40 deg^2 BCS5h30 field. (Note that this number differs from the number of sources detected in a preliminary map and masked in the timestream processing. The mapmaking, source flagging, and timestream processing loop was not iterated over.) All pixels within a radius of four times the beam FWHM of the locations of these sources are set to a DC level defined to be the average of the pixels just outside the mask radius. To avoid any edge effects from the masking procedure, pixels within 8′ of a masked source are flagged and excluded from later cluster finding. This technique proved adequate to avoid false detections of decrements near bright positive sources.

The instrumental and atmospheric noise properties of the maps are estimated using the two-dimensional power spectrum of jackknife noise maps (Sayers et al. 2009; Halverson et al. 2009). Under the assumption of stationarity in the map basis, the noise covariance matrix $\tilde{N}_{\rm noise}$ is diagonal in the Fourier domain and equal to the noise power spectrum. We construct an individual jackknife map by multiplying one half of the individual observations (selected randomly) by -1 then coadding the full set of observations. We repeat this process $n > m$ times (where m is the number of individual observations), computing the two-dimensional spatial power spectrum for each individual jackknife map. The mean of these power spectra is our estimate of $\tilde{N}_{\rm noise}$.

2.4.3. Significance

The significance of a detection is estimated using the standard deviation of the filtered map pixels while excluding regions around bright point sources. As the integration time per pixel is a weak function of elevation, the scatter is estimated independently for each 1.°5 band in elevation. The coverage of the selected region is uniform in azimuth. We define detection significance as the ratio of the peak of the candidate decrement divided by the rms at the appropriate elevation.

2.5. False Detection Simulations

To assess the likelihood of false detections in our deep 150 GHz maps, we run the cluster detection pipeline over a series of simulated maps. The simulated maps include models of astrophysical contaminants (primary CMB and point sources) and noise. The CMB contribution to the simulated maps is a realization of the WMAP5 CMB power spectrum (Nolta et al. 2009). The point-source contribution is a spatially random distribution of sources drawn from models based on the Borys et al. (2003) counts for dusty protogalaxies and a version of the Toffolatti et al. (1998) counts for radio-loud active galactic nuclei (AGNs) modified to match the DASI, CBI, and VSA counts at 30 GHz (Kovac et al. 2002; Mason et al. 2003; Cleary et al. 2005). (As predicted in Section 2.4.2, the contribution of the unresolved AGN population to the power in the simulated maps turns out to be negligible.) Both the CMB and point-source contributions are spatially filtered to mimic the effect of our beams and most of our timestream processing. The effect of the common-mode subtraction is not included. The noise in the simulated maps is created using a jackknife procedure identical to the one described in Section 2.4.2. As with the real data, clusters are searched for in each of the 14 filtered versions of each simulated map, using a β-model source template with $\beta = 1$ and $\theta_{\rm core}$ ranging from 0.′25 to 3.′5 in 0.′25 steps. In 100 simulated maps, we incur an average of 0.02 false detections per

Table 1
Cluster Detections

ID	R.A.	Decl.	S/N at 150 GHz	95 GHz	225 GHz	Best $\theta_{\rm core}$	Best $y_0 \times 10^4$
SPT-CL 0517-5430	79.144	−54.506	−8.8	−3.4	−0.4	1.′5	0.97 ± 0.13
SPT-CL 0547-5345	86.650	−53.756	−7.4	−3.9	1.9	0.′5	1.31 ± 0.21
SPT-CL 0509-5342	77.333	−53.702	−6.0	−3.4	0.1	1.′25	0.67 ± 0.12
SPT-CL 0528-5300	82.011	−52.998	−5.6	−2.6	−1.3	0.′5	1.00 ± 0.19

Notes. R.A. and decl. are in units of degrees (J2000). The value of $\theta_{\rm core}$ reported here is that which maximized the S/N of each cluster in the filtered 150 GHz maps (out of the 14 values of $\theta_{\rm core}$ in steps of 0.′25) and should be interpreted only as a rough measure of that cluster's angular scale. The value of y_0 reported for each cluster is the value in the 150 GHz map filtered at the best values of $\theta_{\rm core}$. The uncertainty on the value of y_0 is calculated for $\theta_{\rm core}$ fixed at the best value. Once we fix β and $\theta_{\rm core}$, y_0 is the only remaining free parameter, so the fractional uncertainty on y_0 is simply equal to the inverse of the 150 GHz S/N in quadrature with the 150 GHz calibration uncertainty.

40 deg^2 for the signal-to-noise ratio (S/N) of the least significant cluster candidate listed in Table 1 and Figure 1. Furthermore, a disproportionately large fraction of the false detections occur when the simulated maps are filtered with the smallest scale optimal filter—which is not surprising, given that there are more independent resolution elements in this filtered map than in the maps filtered for detection of larger-scale objects. If we restrict the filtering of the simulated maps to the scales on which the four clusters in Table 1 are most effectively detected, the false rate above 5.5σ drops below 0.01 per 40 deg^2.

3. RESULTS

In this section, we present the four highest significance cluster candidates found by our matched filter in the 150 GHz map of the ∼40 deg^2 BCS5h30 field. The highest significance candidate in our field was previously identified as a cluster in the Abell supplementary southern catalog (Abell et al. 1989), in which it is identified as AS0520, and in the *ROSAT*-ESO Flux Limited X-ray (REFLEX) survey (Böhringer et al. 2004), in which it is identified as RXCJ0516.6-5430. The remaining three cluster candidates are new discoveries. Based on the simulated observations described in Section 2.5, there is roughly a 2% chance that our lowest significance detection is false; the chances that any of the top three are false detections are significantly smaller than 1%.

To confirm that these detections have a thermal SZ spectrum, we look in filtered versions of our 95 GHz and 225 GHz maps at the locations of the 150 GHz detections. To check each object at the other two frequencies, we use a single-frequency filtered map—created using a matched filter as described in Section 2.4 with the cluster spatial profile that produced the highest significance for that object in the 150 GHz map—and look at the single map pixel that corresponds to the center of the 150 GHz detection. The use of this method, and the fact that the pixel distributions in the filtered maps are Gaussian to a high degree of precision, allows us to easily interpret the S/N at the cluster candidate locations in the 95 GHz and 225 GHz maps.

The candidate locations, the S/N at that location in the filtered map in each of our observing bands, the value of $\theta_{\rm core}$ that maximized the S/N at 150 GHz, and the value of the best-fit central Comptonization parameter, y_0, for that value of $\theta_{\rm core}$ are presented in Table 1. We emphasize that this value of $\theta_{\rm core}$ is the result of a search over a very coarse grid in parameter space using a model that may not be an accurate description of the detailed cluster morphology. It is also reported without a confidence interval. As such, it should be interpreted only as a rough measure of the angular scale of the cluster candidates. Similarly, the value of y_0 and the uncertainty on that value reported in the table are the results of an effective one-parameter fit to the data with β fixed at 1 and $\theta_{\rm core}$ fixed at the grid value that maximized detection significance.

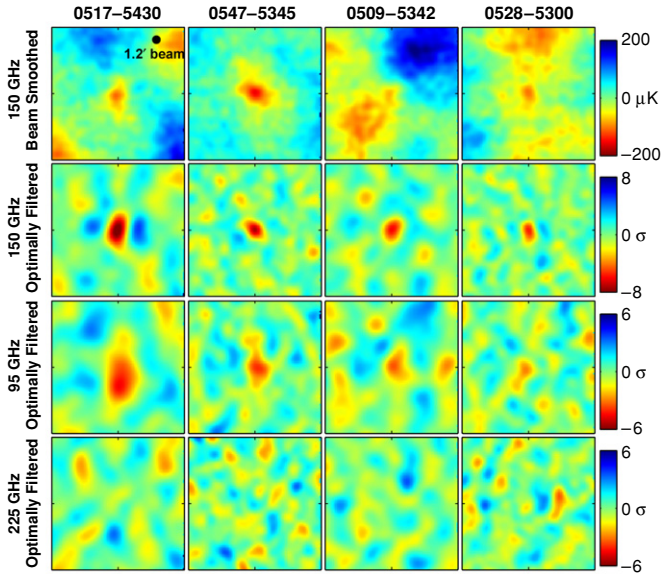

Figure 1. Images of four galaxy clusters found in the SPT SZ survey. In each panel, the region shown is a 20 by 20 arcmin box centered on the cluster. All images are oriented with north up and east to the left. In the top row, we show the beam-smoothed 150 GHz map, and the scale has units of $\mu K_{\rm CMB}$. The lower three rows show the 150, 95, and 225 GHz maps filtered using a $\beta = 1$ model with the $\theta_{\rm core}$ listed in Table 1. The ringing on either side of the cluster in the 150 GHz filtered maps is an artifact of the filtering. The scale gives detection significance in σ. The detections at 95 GHz range in significance from 2.5σ to 3.9σ (see Table 1) and provide supporting evidence for the 150 GHz cluster detections. Our 225 GHz maps are consistent with noise at these four locations (see Table 1 and Section 3), providing another cross-check that the data are consistent with SZ sources. The first cluster shown here, SPT-CL 0517-5430, was previously identified in the REFLEX X-ray cluster survey, in which it is identified as RXCJ0516.6-5430 and in the Abell supplementary southern catalog, in which it is identified as AS0520.

Images of all four candidates in the filtered maps are shown in Figure 1. Two things are immediately evident from the S/N values in the table and the images in the figure: (1) from the significance of the 150 GHz detections alone, all of the candidates are inconsistent with noise fluctuations. (They are also inconsistent with emission from sources such as radio-loud AGNs or dusty protogalaxies because of the polarity of the signal.) (2) From the 95 and 225 GHz images and detection significances, all four detections appear consistent with thermal

SZ signal and inconsistent with primary CMB, since each candidate is significantly detected in the 95 GHz map but not in the 225 GHz map.

We can make this second statement more quantitative. Using the relative depths of our 150 GHz and 95 GHz maps and the frequency dependence of the thermal SZ effect, we can make a prediction for the detection significance at 95 GHz from the 150 GHz detections and for the expected rms deviation (due to noise and calibration uncertainty) between our predicted and observed values. Taking into account the absolute calibration uncertainty in each band (as estimated in Section 2.3.2) and assuming the calibration errors are uncorrelated between bands, the expected signal at 95 GHz given our 150 GHz measurement is

$$T_{95}(\mathrm{pred.}) = T_{150}\frac{f_{\mathrm{SZ}}(95)}{f_{\mathrm{SZ}}(150)}, \quad (3)$$

with an uncertainty of

$$\sigma(T_{95}, \mathrm{pred.}) = \sqrt{\sigma_{150}^2 + (\delta_{\mathrm{cal},150}T_{150})^2}\,\frac{f_{\mathrm{SZ}}(95)}{f_{\mathrm{SZ}}(150)}, \quad (4)$$

where σ_{150}^2 is the noise in the optimally filtered 150 GHz map, $\delta_{\mathrm{cal},150}$ is the calibration uncertainty at 150 GHz, and $f_{\mathrm{SZ}}(\nu)$ is the value of the frequency-dependent thermal SZ brightness relative to the CMB background at frequency ν (in GHz). Similarly, the uncertainty in the observed 95 GHz signal is

$$\sigma(T_{95}, \mathrm{obs.}) = \sqrt{\sigma_{95}^2 + (\delta_{\mathrm{cal},95}T_{95})^2}. \quad (5)$$

The expected deviation between the predicted and observed values of the 95 GHz S/N for a single cluster candidate will be the quadrature sum of the above uncertainty terms, divided by the 95 GHz noise:

$$\left\langle(\Delta(\mathrm{S/N})_{95})^2\right\rangle = 1 + (\delta_{\mathrm{cal},95}(\mathrm{S/N})_{95})^2 + \left(\frac{f_{\mathrm{SZ}}(95)}{f_{\mathrm{SZ}}(150)}\frac{\sigma_{150}}{\sigma_{95}}\right)^2 \times \left[1 + (\delta_{\mathrm{cal},150}(\mathrm{S/N})_{150})^2\right]. \quad (6)$$

The rms is approximately 4.8 times higher in CMB fluctuation temperature units in our 95 GHz map than in our 150 GHz map, but in those same units the thermal SZ signal should be approximately 1.6 times stronger at 95 GHz. Using these values, the predicted 95 GHz S/N values for our four candidates are −3.0, −2.5, −2.0, and −1.9, as compared to the observed values of −3.4, −3.9, −3.4, and −2.6 (compare Table 1). Using Equation (6), the rms deviation between the predicted and observed 95 GHz S/N should be 1.2, 1.2, 1.2, and 1.1 for the four candidates. Taking into account the correlated nature of the calibration contribution in Equation (6), a χ^2 test for the difference between the predicted and observed 95 GHz S/N values produces a probability to exceed (PTE) of 0.66.

Because our 225 GHz band is near the thermal SZ null ($f_{\mathrm{SZ}}(225) \simeq 0.1$), we should see very little signal at cluster locations in our 225 GHz map, and the 225 GHz equivalents to the last two terms in Equation (6) should vanish. For this reason, and because the observed 225 GHz S/N values are quite small, the expected rms deviation between the predicted and observed 225 GHz S/N should be very close to unity, and the deviations should be almost uncorrelated between cluster candidates. A χ^2 test for the observed S/N at 225 GHz produces a PTE of 0.30.

We can do a similar exercise for the hypothesis that the observed signal has a 2.7 K thermal spectrum (as would be the case for primary CMB fluctuations) by replacing the f_{SZ} ratio in Equation (6) with unity (because the maps are calibrated to be in units of equivalent CMB fluctuation temperature). In this case, the PTE for 95 GHz is still non-negligible (∼0.09), because the difference between the spectra of thermal SZ and primary CMB is not so great between 95 and 150 GHz. However, given the depth of the 225 GHz map (the rms in CMB fluctuation temperature is approximately 2.5 times that in the 150 GHz map), we would expect S/N values of −3.5, −3.0, −2.4, and −2.2 at 225 GHz for a 2.7 K thermal spectrum. The PTE for this model given the observed S/N values at 225 GHz is $\sim 6 \times 10^{-6}$, giving strong evidence that the signal spectrum of our cluster candidates is inconsistent with primary CMB but consistent with thermal SZ.

3.1. X-ray Counterparts

As previously mentioned, the highest significance cluster candidate in our sample (SPT-CL 0517-5430) was identified as a galaxy cluster in the REFLEX survey, which selected cluster candidates by correlating sources from a *ROSAT* All-Sky Survey (RASS; Truemper 1993) catalog with galaxy locations from optical data. Interestingly, we also find RASS counterparts to two of our other three cluster candidates, but these sources have not previously been considered as X-ray cluster candidates. The sources are found in the RASS Faint Source Catalog (RASS-FSC; Voges et al. 2000), and each lies within 1 arcmin of one of our SZ-detected clusters. 1RXS J054638.7−534434 lies 0.9 arcmin northeast of SPT-CL 0547-5345, while 1RXS J050921.2−534159 lies 0.2 arcmin northeast of SPT-CL 0509-5342 (see Figure 3). The combined number density of RASS Bright Source Catalog (Voges et al. 1999) and RASS-FSC sources in the BCS5h30 field is 6.6 deg^{-2} (roughly twice the 3.0 deg^{-2} all-sky average), which makes the likelihood of a chance superposition within 1 arcmin of a random location in the BCS5h30 field less than 0.6%. The RASS-FSC count rates in the broad energy band are 0.012 counts s^{-1} for 1RXS J054638.7−534434 and 0.035 counts s^{-1} for 1RXS J050921.2−534159. The count rates are both well below the flux threshold used in the REFLEX survey, which is approximately 0.08 counts s^{-1} in a slightly narrower energy band. Using the RASS-FSC exposure times and count rates, we estimate that both of these sources were detected with roughly 15 photons in the broad energy band. Neither of these sources would have been included in the Massive Cluster Survey (Ebeling et al. 2001), which only considered sources in the RASS-BSC. We find no X-ray counterpart in the literature or in publicly available catalogs for our cluster candidate SPT-CL 0528-5300.

3.1.1. Positional Uncertainties in SPT SZ Cluster Detections

As discussed in Section 2.3.4, the absolute pointing of the SPT maps from which cluster candidates are extracted is accurate to roughly 10 arcsec, as measured using sources in the PMN and SUMSS catalogs. However, the locations of the cluster candidates reported in Table 1 will not necessarily line up with the centers of the cluster optical or X-ray emission to that level of precision, because the different observations are sensitive to different combinations of physical properties of the cluster. Such a separation is particularly likely in extended systems and systems that have undergone recent mergers, such as SPT-CL 0517-5430/RXCJ0516.6-5430 (Zhang et al. 2006). The position of the brightest cluster galaxy, the peak of the X-ray emission (which is proportional to electron column density squared), and the center of the SZ emission (which is linearly proportional to

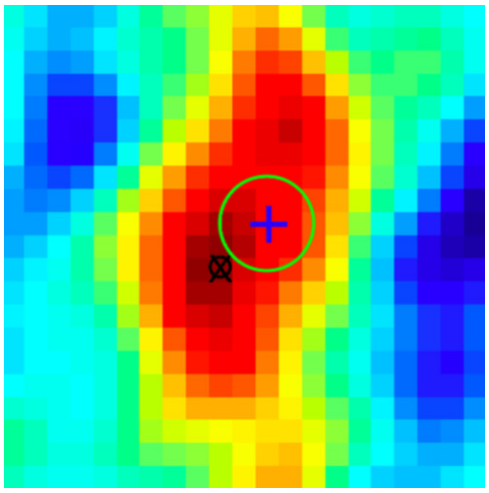

Figure 2. Minimally filtered (beam-smoothed to reduce pixel noise and high-passed to remove the primary CMB) 150 GHz image of SPT-CL 0517-5430, with colors and orientation as in the second row of Figure 1, but zoomed in such that the displayed region is 5 arcmin on a side. The blue cross indicates the position of the peak of the output of the matched filter, i.e., the peak of the filtered 150 GHz image shown in Figure 1, which is also the position reported in Table 1. The black X and circle indicate the position of RXCJ0516.6-5430, as reported in the REFLEX survey (Böhringer et al. 2004) and the positional uncertainty of the associated source in the RASS Bright Source Catalog (Voges et al. 1999). The green circle around the SZ detection center is 1 arcmin in diameter as in Figure 3, which also shows the REFLEX position.

electron column density and is smoothed by the matched filter used for detection) can be offset by many times the positional uncertainty in any of the three measurements.

Figure 2 shows a minimally filtered version of the 150 GHz image in Figure 1, and it clearly shows the offset between the center of the diffuse SZ emission and the deepest part of the SZ decrement. The extent of the deepest part of the SZ decrement is $\sim 1'$, and it is detected as a separate feature at 2–3σ in this version of the 150 GHz map, indicating that the $\sim 0.'7$ offset between the SZ centroid and the deepest part of the decrement is statistically significant. The X-ray emission should be strongly peaked in this deepest part of the decrement, and indeed this is where the reported REFLEX position is located.

3.2. Optical Counterparts

We examine the galaxy distributions at the locations of the SZ-selected clusters using deep, multiband optical images from the BCS. The BCS is a 60 night NOAO survey program (2005–2008) on the Blanco 4 m that has uniformly imaged 75 deg^2 of the sky in SDSS $griz$ bands in preparation for cluster finding with SPT and other millimeter-wave experiments. The depths in each band are tuned to follow cluster L_* galaxies to $z = 1$ with $>10\sigma$ detections. In addition to the large science fields, BCS covers seven small fields that overlap large spectroscopic surveys so that the photometric redshifts (photo-z's) using BCS data can be trained and tested using a sample of over 5000 galaxies.

Figure 3 shows pseudo-color images created from deep BCS gri coadded images of the four systems. Early-type galaxies at similar redshift appear with similar color in these pseudo-color images. The clusters are arranged counter-clockwise by redshift starting in the upper left. In these images the galaxy populations in SPT-CL 0517-5430 and SPT-CL 0509-5342 are yellow, and the much fainter, higher-redshift populations in SPT-CL 0528-5300 and SPT-CL 0547-5345 are orange and red. In each image, the SPT position is marked with a 1 arcmin diameter green circle.

We have used ANNz (Collister & Lahav 2004) photo-z's and color–magnitude diagrams to probe for a cluster galaxy population and to provide rough redshift estimates for each of the SPT systems. A full analysis of the optical properties of these clusters that includes comparison to clusters selected by other means will appear in a separate paper. Here, we provide a short summary of our findings.

In SPT-CL 0517-5430, the cluster that was previously included in the Abell supplementary southern cluster catalog (Abell et al. 1989) and the REFLEX catalog (Böhringer et al. 2004), there is a strong red sequence population apparent in $g-r$ versus r and a peak in the photo-z histogram. Both indicate a redshift of $z \sim 0.35$, which is roughly consistent with the value of $z = 0.295$ quoted in Böhringer et al. (2004). The dominant elliptical is $0.'5$ to the northeast of the SPT position (see Figure 3).

In SPT-CL 0509-5342 the central dominant elliptical is clearly visible $\sim 0.'25$ to the southeast of the SPT position. This galaxy is marked by two and perhaps three strong gravitational lensing arcs. A large population of similarly colored and less luminous galaxies is apparent in the image and show up clearly as a red sequence in the $r-i$ versus i color–magnitude diagram. The red sequence indicates a cluster redshift of $z \sim 0.45$, while the photo-z histogram shows a peak around $z \sim 0.4$, but also several peaks at higher redshift.

SPT-CL 0528-5300 has a much fainter galaxy population at higher redshift, and it appears more concentrated on the sky. The cluster core is $\sim 0.'4$ east of the SPT position, and the cluster galaxies appear orange in Figure 3. This cluster has a red sequence visible in $r-i$ versus i and in $i-z$ versus z suggesting a redshift of $z \sim 0.8$, again consistent with the location of a strong peak in the photo-z histogram.

SPT-CL 0547-5345 is the highest redshift system; its galaxy population is faint and red in Figure 3. The cluster core is located $\sim 0.'25$ to the southeast of the SPT position. Inspection of the images reveals a large population of faint galaxies that are not readily apparent in the figure. The red sequence is not clearly detected for this cluster. We note, however, that the galaxies for this cluster are close to the detection limit and therefore statistical uncertainties in their photometry are likely to be an issue. The photo-z histogram shows a peak at $z \sim 0.9$, very close to the high redshift range measured for the entire field. A feature that appears to be a strong gravitational lensing arc lies near the SPT circle to the southwest of the SPT position.

The BCS optical data reveal galaxy concentrations located within $0.'5$ of the SPT position for each of the four clusters. We find that the cluster red sequence is present in all but the highest redshift system and gravitational lensing arcs are present in two of the SPT systems, including the highest redshift cluster.

We also note that the trend in cluster angular size—as evident from the images in Figure 1 and the rough estimate of $\theta_{\rm core}$ in Table 1—is consistent with the redshift estimates presented in this section. The two clusters estimated to lie at $z \gtrsim 0.8$ are noticeably more compact and prefer smaller values of $\theta_{\rm core}$ than the clusters estimated to lie at $z \sim 0.4$.

4. CONCLUSIONS

In this paper, we have reported four high-significance detections of galaxy clusters made with the SPT, three of which are new discoveries. These clusters were identified first as Sunyaev–Zel'dovich effect decrements in 150 GHz SPT maps. The presence of decrements at the corresponding positions in the 95 GHz maps, and lack of signal at the same positions in the 225 GHz

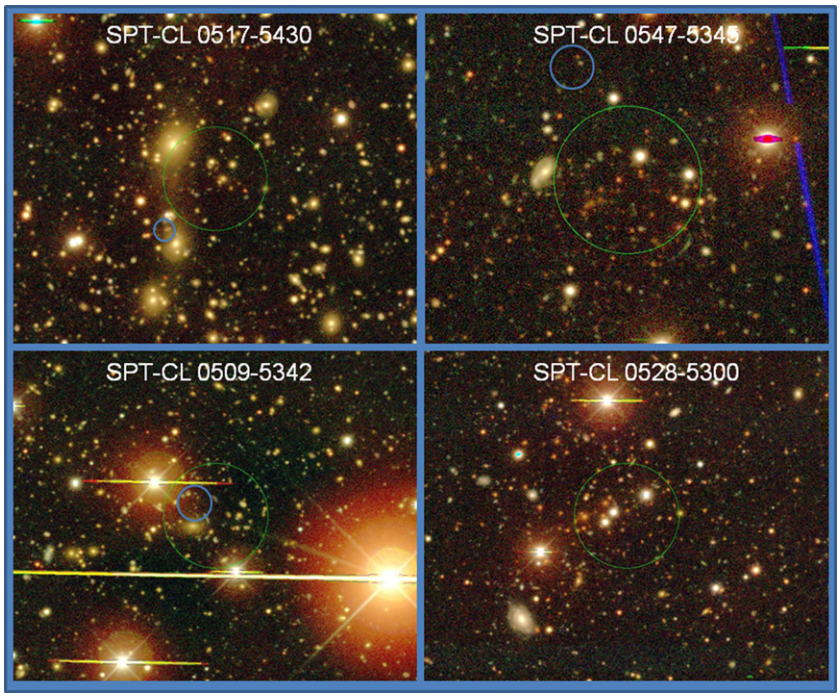

Figure 3. Pseudo-color optical images of the galaxy distributions toward the SPT clusters. All images are oriented with north up and east to the left, as in Figures 1 and 2. The SPT position is marked with a 1 arcmin diameter green circle, as in Figure 2. Populations of early-type galaxies with similar color and central giant elliptical galaxies are found to lie within 0.′5 of the SPT position of each system. Gravitational lensing arcs are apparent near the central galaxy in SPT-CL 0509-5342 and to the southwest of the cluster core in SPT-CL 0547-5345. The REFLEX position for SPT-CL 0517-5430/RXCJ0516.6-5430 is indicated with a blue circle in the upper left panel, as are the positions of the possible RASS counterparts for SPT-CL 0547-5345 and SPT-CL 0509-5342 in their respective images. The diameter of each blue circle is equal to the positional error given for that source in the RASS Faint Source Catalog.

maps, supports their identification as SZ sources. One of these four systems was previously identified as a cluster in the Abell supplementary southern catalog and the REFLEX X-ray cluster catalog. Two of the others have potential RASS Faint Source Catalog counterparts, but had not been identified as clusters. We have used data from the Blanco Cosmology Survey to produce pseudo-color optical images in the direction of the four SZ detections and find clear galaxy overdensities within 1 arcmin of the reported SPT positions. We also see evidence for strong gravitational lensing arcs in at least two of the optical images. Preliminary photometric redshift estimates indicate that two of the systems lie at moderate redshift ($z \sim 0.4$) and two at high redshift ($z \gtrsim 0.8$), consistent with the rough estimate of cluster angular scale from the SZ detections.

The cluster search presented in this paper was performed over a $\sim$40 deg^2 subfield of the SPT survey region observed in both the 2007 and 2008 seasons. The SPT is expanding the survey coverage, with an eventual target of $\geqslant$1000 deg^2. Future analysis will include additional data, as well as improvements to the data processing, calibration, and cluster identification algorithms. These initial cluster detections demonstrate the potential of SZ effect surveys, and in particular the SPT, to produce a sample of SZ-selected galaxy clusters. In combination with optical and X-ray data, these and future SZ-selected clusters will enable new explorations of galaxy cluster properties and constraints on cosmological models.

The SPT team gratefully acknowledges the contributions to the design and construction of the telescope by S. Busetti, E. Chauvin, T. Hughes, P. Huntley, and E. Nichols and his team of iron workers. We also thank the National Science Foundation (NSF) Office of Polar Programs, the United States Antarctic Program and the Raytheon Polar Services Company for their support of the project. We are grateful for professional support from the staff of the South Pole station. We acknowledge S. Alam, W. Barkhouse, S. Bhattacharya, M. Brodwin, L. Buckley-Greer, S. Hansen, W. High, H. Lin, Y-T Lin, A. Rest, C. Smith, and D. Tucker for their contribution to BCS data acquisition, and we acknowledge the DESDM team, which has developed the tools we used to process and calibrate the BCS data. We thank M. Brodwin, A. Gonzalez, J. Song, and C. Stubbs for their advice and contributions in the optical analysis. The BCS is supported by NSF awards AST 05-07688 and AST 07-08539. DESDM development is supported by NSF awards AST 07-15036 and AST 08-13534. We thank J. Leong, W. Lu, M. Runyan, D. Schwan, M. Sharp, and C. Greer for their early contributions to the SPT project and J. Joseph and C. Vu for their contributions to the electronics.

The South Pole Telescope is supported by the National Science Foundation through grants ANT-0638937 and ANT-0130612. Partial support is also provided by the NSF Physics Frontier Center grant PHY-0114422 to the Kavli Institute of Cosmological Physics at the University of Chicago, the Kavli Foundation and the Gordon and Betty Moore Foundation. The McGill group acknowledges funding from the National Sciences and Engineering Research Council of Canada, the Quebec Fonds de recherche sur la nature et les technologies, and the Canadian Institute for Advanced Research. The following individuals acknowledge additional support: A.L. from the Brinson Foundation; K.S. from a KICP Fellowship; J.M. from a Fermi Fellowship; Z.S. from a GAAN Fellowship; A.T.L. from the Miller Institute for Basic Research in Science, University of California, Berkeley; and N.W.H. from an Alfred P. Sloan Research Fellowship.

REFERENCES

Abell, G. O., Corwin, H. G., Jr., & Olowin, R. P. 1989, ApJS, 70, 1
Benson, B. A., Church, S. E., Ade, P. A. R., Bock, J. J., Ganga, K. M., Henson, C. N., & Thompson, K. L. 2004, ApJ, 617, 829
Birkinshaw, M. 1999, Phys. Rep., 310, 97
Böhringer, H., et al. 2004, A&A, 425, 367
Bonamente, M., Joy, M. K., LaRoque, S. J., Carlstrom, J. E., Reese, E. D., & Dawson, K. S. 2006, ApJ, 647, 25
Borys, C., Chapman, S., Halpern, M., & Scott, D. 2003, MNRAS, 344, 385
Calabretta, M. R., & Greisen, E. W. 2002, A&A, 395, 1077
Carlstrom, J. E., Holder, G. P., & Reese, E. D. 2002, ARA&A, 40, 643
Carlstrom, J. E., et al. 2009, PASP, submitted
Cleary, K. A., et al. 2005, MNRAS, 360, 340
Coble, K., et al. 2003, arXiv:astro-ph/0301599
Collister, A. A., & Lahav, O. 2004, PASP, 116, 345
Ebeling, H., Edge, A. C., & Henry, J. P. 2001, ApJ, 553, 668
Haehnelt, M. G., & Tegmark, M. 1996, MNRAS, 279, 545
Haiman, Z., Mohr, J. J., & Holder, G. P. 2001, ApJ, 553, 545
Halverson, N. W., et al. 2009, ApJ, in press (arXiv:0807.4208)
Herranz, D., Sanz, J. L., Barreiro, R. B., & Martínez-González, E. 2002a, ApJ, 580, 610
Herranz, D., Sanz, J. L., Hobson, M. P., Barreiro, R. B., Diego, J. M., Martínez-González, E., & Lasenby, A. N. 2002b, MNRAS, 336, 1057
Holder, G., Haiman, Z., & Mohr, J. J. 2001, ApJ, 560, L111
Holzapfel, W. L., Carlstrom, J. E., Grego, L., Joy, M., & Reese, E. D. 2000, ApJ, 539, 67
Jones, M. E., et al. 2005, MNRAS, 357, 518
Kovac, J. M., Leitch, E. M., Pryke, C., Carlstrom, J. E., Halverson, N. W., & Holzapfel, W. L. 2002, Nature, 420, 772
Lima, M., & Hu, W. 2007, Phys. Rev. D, 76, 123013
Majumdar, S., & Mohr, J. J. 2004, ApJ, 613, 41
Mason, B. S., et al. 2003, ApJ, 591, 540
Mauch, T., Murphy, T., Buttery, H. J., Curran, J., Hunstead, R. W., Piestrzynski, B., Robertson, J. G., & Sadler, E. M. 2003, MNRAS, 342, 1117
Melin, J.-B., Bartlett, J. G., & Delabrouille, J. 2005, A&A, 429, 417
Melin, J.-B., Bartlett, J. G., & Delabrouille, J. 2006, A&A, 459, 341
Molnar, S. M., Haiman, Z., Birkinshaw, M., & Mushotzky, R. F. 2004, ApJ, 601, 22
Motl, P. M., Hallman, E. J., Burns, J. O., & Norman, M. L. 2005, ApJ, 623, L63
Nagai, D. 2006, ApJ, 650, 538
Nagai, D., Kravtsov, A. V., & Vikhlinin, A. 2007, ApJ, 668, 1
Navarro, J. F., Frenk, C. S., & White, S. D. M. 1996, ApJ, 462, 563
Navarro, J. F., Frenk, C. S., & White, S. D. M. 1997, ApJ, 490, 493
Nolta, M. R., et al. 2009, ApJS, 180, 296
Padin, S., et al. 2008, Appl. Opt., 47, 4418
Reichardt, C. L., et al. 2009, ApJ, 694, 1200
Richards, E. A., Fomalont, E. B., Kellerman, K. I., Partridge, R. B., & Windhorst, R. A. 1997, AJ, 113, 1475
Ruhl, J., et al. 2004, Proc. SPIE, 5498, 11
Runyan, M. C., et al. 2003, ApJS, 149, 265
Sayers, J., et al. 2009, ApJ, 690, 1597
Shaw, L. D., Holder, G. P., & Bode, P. 2008, ApJ, 686, 206
Sunyaev, R. A., & Zeldovich, Y. B. 1970, Comments Astrophys. Space Phys., 2, 66
Sunyaev, R. A., & Zeldovich, Y. B. 1972, Comments Astrophys. Space Phys., 4, 173
Toffolatti, L., Argueso Gomez, F., de Zotti, G., Mazzei, P., Franceschini, A., Danese, L., & Burigana, C. 1998, MNRAS, 297, 117
Truemper, J. 1993, Science, 260, 1769
Voges, W., et al. 1999, A&A, 349, 389
Voges, W., et al. 2000, VizieR Online Data Catalog 9029, 0
Wang, S., Khoury, J., Haiman, Z., & May, M. 2004, Phys. Rev. D, 70, 123008
Wang, L., & Steinhardt, P. J. 1998, ApJ, 508, 483
White, M., & Majumdar, S. 2004, ApJ, 602, 565
Wright, A. E., Griffith, M. R., Burke, B. F., & Ekers, R. D. 1994, ApJS, 91, 111
Zhang, Y.-Y., Böhringer, H., Finoguenov, A., Ikebe, Y., Matsushita, K., Schuecker, P., Guzzo, L., & Collins, C. A. 2006, A&A, 456, 55